Tail domains of myosin-1e regulate phosphatidylinositol signaling and F-actin polymerization at the ventral layer of podosomes

Yage Zhang[a,†], Fakun Cao[a,†], Yuhuan Zhou[a], Zhen Feng[a], Brian Sit[a,b], Mira Krendel[c], and Cheng-han Yu[a,*]

[a]School of Biomedical Sciences, Faculty of Medicine, University of Hong Kong, Hong Kong; [b]Randall Division of Cell and Molecular Biophysics, Faculty of Life Sciences and Medicine, King's College London, London WC2R 2LS, United Kingdom; [c]SUNY Upstate Medical University, Syracuse, NY 13210

ABSTRACT During podosome formation, distinct phosphatidylinositol 3,4,5-trisphosphate lipid (PI(3,4,5)P3) production and F-actin polymerization take place at integrin-mediated adhesions. Membrane-associated actin regulation factors, such as myosin-1, serve as key molecules to link phosphatidylinositol signals to podosome assembly. Here, we report that long-tailed myosin-1e (Myo1e) is enriched at the ventral layer of the podosome core in a PI(3,4,5)P3-dependent manner. The combination of TH1 and TH2 (TH12) of Myo1e tail domains contains the essential motif for PI(3,4,5)P3-dependent membrane association and ventral localization at the podosome. TH12 KR2A (K772A and R782A) becomes dissociated from the plasma membrane. While F-actin polymerizations are initialized from the ventral layer of the podosome, TH12 precedes the recruitment of N-WASP and Arp2/3 in the initial phase of podosome formation. Overexpression of TH12, not TH12 KR2A, impedes PI(3,4,5)P3 signaling, restrains F-actin polymerization, and inhibits podosome formation. TH12 also suppresses gelatin degradation and migration speed of invadopodia-forming A375 melanoma cells. Thus, TH12 domain of Myo1e serves as a regulatory component to connect phosphatidylinositol signaling to F-actin polymerization at the podosome.

INTRODUCTION

Cell-matrix adhesion formation involves extracellular ligand binding, as well as intracellular signal transduction (Hynes, 2002; Schiller and Fassler, 2013). Adhesion signaling at integrin receptors on the plasma membrane can promote cytoskeletal remodeling, cell migration, and matrix reorganization (Eyckmans et al., 2011; Case and Waterman, 2015). Podosomes and invadopodia are integrin-mediated adhesions that are usually found in macrophages and invasive cancer cells (Buccione et al., 2004; Murphy and Courtneidge, 2011). These cells exhibit matrix metalloproteinase activities and can degrade extracellular matrices in proximity to the adhesion sites (Castro-Castro et al., 2016; El Azzouzi et al., 2016). During the formation of podosomes, there is a distinct F-actin polymerization at the center of each podosome (podosome core) surrounded by adhesion-related proteins (podosome ring; van den Dries et al., 2013; Yu et al., 2013; Labernadie et al., 2014). N-WASP and Arp2/3 are the key factors to trigger F-actin polymerization at the podosome core. Various F-actin regulating molecules and motor proteins, such as myosin1e (Myo1e) are also located at the podosome (Ouderkirk and Krendel, 2014).

Phosphatidylinositol (PI) lipids and its derivatives often serve as important signal messengers in the plasma membrane (Goley and Welch, 2006; Takenawa and Suetsugu, 2007). Through the activation of PI-specific kinases, the inositol ring in the head group of PI can be phosphorylated at the third, fourth, and fifth hydroxyl groups. In the plasma membrane, phosphatidylinositol 4,5-bisphosphate (PI(4,5)P2), phosphatidylinositol 3,4-bisphosphate (PI(3,4)P2), and phosphatidylinositol 3,4,5-trisphosphate (PI(3,4,5)P3) often serve as

upstream signals to regulate a wide variety of cellular events, such as cell proliferation and cell migration (Di Paolo and De Camilli, 2006; Balla, 2013). Negatively charged PI lipids can locally recruit N-WASP, promote Cdc42-GTP level, and activate Arp2/3-mediated F-actin polymerization (Insall and Weiner, 2001; Papayannopoulos et al., 2005; Park et al., 2008). The activation of PI-specific kinase can be mediated by various signal pathways. For example, the introduction of constitutively active Src mutant can promote phosphoinositide 3-kinase (PI3K) activation (Oikawa et al., 2008; Hoshino et al., 2012). PI3K activation at integrin-mediated adhesions can trigger the production of PI(3,4,5)P3 and plays an essential role in the formation of podosomes (Yamaguchi et al., 2011; Yu et al., 2013).

Class 1 myosins are known to play important roles in regulating lipid signaling and cytoskeletal reorganization on the plasma membrane (McIntosh and Ostap, 2016). Mammalian class 1 myosins are membrane-associated motor proteins and consist of eight different members (Myo1a to Myo1h; McConnell and Tyska, 2010; McIntosh and Ostap, 2016). All myosin1s contain the conserved large ATPase motor domain (head domain) at the amino terminus that can move along actin filaments by hydrolyzing ATP. The tail domains at the carboxy terminus of myosin1s vary among isoforms and contain functional motifs for lipid and protein interactions (Krendel et al., 2007; Yu and Bement, 2007; Chen et al., 2012; Cheng et al., 2012; Gupta et al., 2013). The neck domain between the head and tail domains contains IQ motifs for calmodulin binding and motor regulation (Lu et al., 2015). Among all myosin1 isoforms, Myo1e is the only long-tail isoform that is ubiquitously expressed. Myo1f is the other long-tail isoform with 82% sequence similarity to Myo1e and mainly expresses in hematopoietic cell lineages. The long tail of Myo1e comprises three tail homology domains, TH1, TH2, and TH3. Whereas TH1 is presented in all myosin1 isoforms and generally contains a pleckstrin homology (PH) domain, actual TH1 sequences between long-tail and short-tail myosin1 isoforms are notably different from each other. TH2 and TH3 are unique domains that follow TH1 in Myo1e's long tail. Unlike other short-tail myosin1 isoforms, Myo1e is uniquely enriched at the podosomes (Cervero et al., 2012; Yu et al., 2013; Ouderkirk and Krendel, 2014). Nevertheless, the role of Myo1e and its C-terminal tail domains at the podosome remains unclear. Here, we reveal the spatial, temporal, and functional role of mammalian Myo1e in podosome-forming Src-transformed fibroblasts (MEF-Src), RAW267.4 macrophages, and A375 melanoma cells.

RESULTS

Ventral enrichment of Myo1e at the podosome

To characterize the three-dimensional distribution of Myo1e at the podosome, we employed Src-transformed fibroblast cells as a model system. Unlike short-lived podosomes in macrophages, mouse embryonic fibroblast cells transfected with constitutive activated Src-Y530F (MEF-Src) spontaneously assembled large and long-lived podosome rosettes and arcs. Dense F-actin assembly surrounded by adhesion proteins in MEF-Src was often stable within 5 min. Stable podosome structures allowed us to monitor and analyze the axial distribution and temporal dynamics of various podosome core components. Each core component with a fluorescent protein tag and a reference marker of F-actin were pairwise examined by spinning-disk confocal microscopy (Figure 1A). Acquired z-stack images were then analyzed with a home-written ImageJ macro and Matlab code. MaxZ, a self-defined parameter presented the axial position with the highest intensity (Figure 1B). We found that β-actin and F-actin marker (calponin homology domain of utrophin [UtrCH], Lifeact, phalloidin) exhibit similar axial distribution with

MaxZ values of 400 nm in each podosome (Supplemental Figure S1A). Therefore, F-actin labeled by UtrCH was utilized as the spatial reference to compare the axial distribution of 26 other podosome core components, including Myo1e, β-actin, filament nucleating factors (Arp3, Cortactin, CARMIL1, Coronin1b, N-WASP, Arpin [inhibitory role]), G-actin–binding proteins (ABP1, CAP1, WIP, Profilin1), depolymerizing factors (Twinfilin1, Cofilin1, Gelsolin), capping proteins (EPS8, CD2AP, CapZ-beta2, CAPG, TMOD3), and cross-linking proteins (Plastin3, VASP, Mena, Alpha-actinin1, FilaminA, Fascin1; Siripala and Welch, 2007; Pollard, 2016). Normalized axial distributions of each podosome core component between 0 and 2 μm were jointly evaluated (Figure 1C and Supplemental Figure S1, B and C). While all core components laterally colocalized at the podosome, their axial distributions in the podosomes were distinctly different (Supplemental Figure S2). In particular, we found that Myo1e was enriched at the ventral layer of podosomes (Figure 1D), as MaxZ of Myo1e was lowest (0.128 ± 0.014 μm, SEM, n = 53; Supplemental Figure S1C). Filament nucleating factors (such as Arp3) were also located in the lower part of the podosome core. On the other hand, cross-linking and pointed-end capping proteins (such as FilaminA and TMOD3, respectively) were situated in the middle and upper part of the podosome core. The distinct enrichment at the ventral layer of the podosome suggests the close Myo1e–plasma membrane interaction at the podosome.

F-actin polymerizes from the ventral layer of the podosome

A three-dimensional rod-like assembly of a dense F-actin network extending from the plasma membrane into the cytosol was one of the prominent characteristics of the podosome. We utilized photoconvertible mEOS2-β-actin to examine the assembly process of F-actin along the axial orientation of the podosome. Spot activation of a 405-nm laser was initiated over a small region away from the podosome. Photoconverted cytosolic mEOS2-β-actin can diffuse within the cell and subsequently assemble into the F-actin core at the podosome. The axial distribution of newly converted mEOS2-β-actin was then monitored by time-lapse confocal microscopy. Within 5 s postactivation, we found that photoconverted mEOS2-β-actin started to incorporate into the ventral layer of the podosome and remained absent from the upper layer of the podosome (Figure 1E and Supplemental Movie 1). The intensity of converted mEOS2-β-actin at the upper layer of the podosome gradually increased over time, while the intensity at ventral layer started to decrease (Figure 1F). Bottom-up incorporations of β-actin at the podosome core were supported by the ventral enrichment of various actin regulators, such as nucleation factor Arp3 and barbed-end capping EPS8 (Figure 1C). It appears that F-actin polymerizes from the ventral layer and moves toward the apical part of the podosome.

PI(3,4,5)P3 lipids recruit Myo1e to the podosome

In MEF-Src, endogenous Myo1e and transfected Myo1e tagged with an N-terminal fluorescent protein were found at the podosome core, as well as the plasma membrane of filopodia protrusions at the outer region of the podosome arc (Figure 2A). Myo1e E393A (a point mutation in the conserved myosin ATPase motor domain that disrupts the salt bridge between switch I and switch II and destabilizes ATP and actin binding [Reubold et al., 2003; Chen et al., 2012]) was also recruited to the podosome and plasma membrane of filopodia protrusions. However, Myo1e without tail domains (Myo1e Δtail, 1-650) and Myo1e-TH1 (1-920, TH2 and TH3 removed) were not enriched at the podosome and had weak association to the filopodia protrusions. As the interaction between lipids and
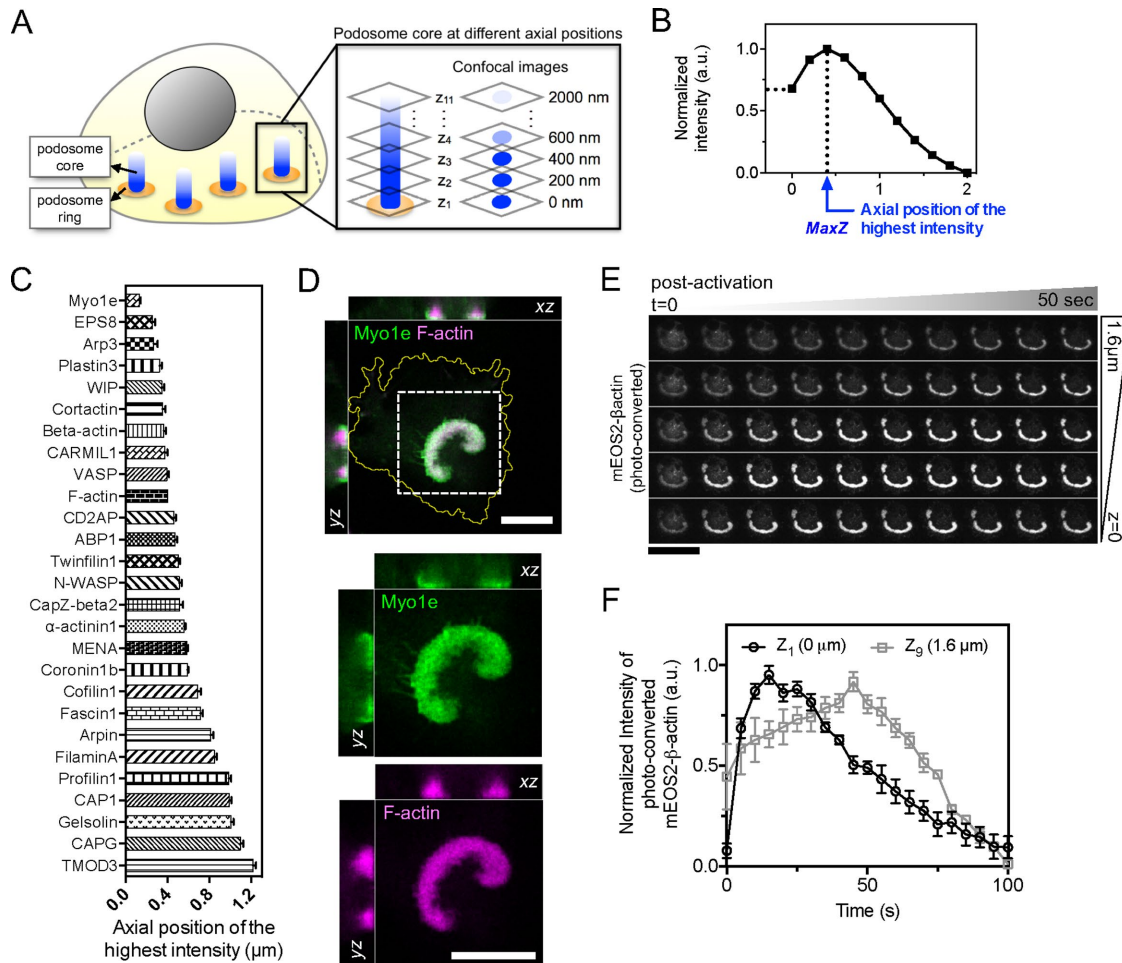
FIGURE 1: Myo1e is enriched at the ventral layer of the podosome core. (A) Schematic of axial distribution analysis of podosome core components. Myo1e, F-actin, and various actin-binding proteins in MEF-Src are imaged by confocal microscopy with 200-nm steps along the z-axis. Images from 0 to 2 μm above the adhesion plane are used for axial distribution analysis. (B) MaxZ, a self-defined parameter, represents the axial position with the highest intensity and is used to compare the axial distribution of each podosome component. (C) MaxZ values of Myo1e, F-actin (labeled by UtrCH), β-actin, and various actin regulators, including filament nucleating factors (Arp3, Cortactin, CARMIL1, Coronin1b, N-WASP, Arpin [inhibitory role]), G-actin–binding proteins (ABP1, CAP1, WIP, Profilin1), depolymerizing factors (Twinfilin1, Cofilin1, Gelsolin), capping proteins (EPS8, CD2AP, CapZ-beta2, CAPG, TMOD3), and cross-linking proteins (Plastin3, VASP, Mena, Alpha-actinin1, FilaminA, Fascin1). Statistical information is in Supplemental Figure S1, B and C. (D) Three-dimensional confocal images of mApple-Myo1e and EBFP2-UtrCH (F-actin marker) in the podosome arc. Inset, the boxed region with the podosome arc (20 × 20 μm²). Myo1e is preferentially distributed at the ventral layer of F-actin. (E) Photoconversion of cytosolic mEOS2-β-actin reveals the dynamics of actin polymerization at the podosome. After 405-nm spot illumination (cyan circle), newly converted mEOS2-β-actin (visualized by 561 nm excitation) are first incorporated into the ventral layer of the podosome. (F) Intensity-time plot of photoconverted mEOS2-β-actin at Z1 (0 μm, ventral layer) and Z9 (1.6 μm above the ventral layer, n = 6). Error bars represent SEM. Scale bars represent 10 μm.

Myo1e has been reported previously, we further examined the composition of phosphatidylinositol lipids at the podosome by various PH-domain–containing probes. PH domains of BTK and PLCδ have been used to specifically monitor the distribution of PI(3,4,5)P3 and PI(4,5)P2, respectively (Di Paolo and De Camilli, 2006). We found that PI(3,4,5)P3 not PI(4,5)P2 lipids were enriched at the ventral layer of the podosome (Figure 2, B and C). As F-actin assembly and podosome formation took place, the PI(3,4,5)P3 level visualized by PH-BTK was gradually increased (Figure 2, D and E, and Supplemental Movie 2). Both catalytic and regulatory subunits of class I PI3K were found at the podosome (Supplemental Figure S3, A and B). On the other hand, the PI(4,5)P2 level, visualized by PH-PLCδ, was

slightly reduced (Figure 2D), and PIP5KI γ661 was not enriched at the podosome core (Supplemental Figure S3C). While both levels of Myo1e and PH-BTK rose progressively during the podosome formation (Supplemental Figure S3, D and E), we tested whether the recruitment of Myo1e at the podosome was dependent on PI(3,4,5)P3 lipids. PTEN (a phosphatidylinositol 3,4,5-bisphosphate 3-phosphatase) and SHIP2 (a phosphatidylinositol 3,4,5-bisphosphate 5-phosphatase) are phosphatases of PI(3,4,5)P3 lipids and can promote the generation of PI(4,5)P2 and PI(3,4)P2, respectively (Dyson et al., 2001). When we overexpressed SHIP2 in MEF-Src, the enrichment level of Myo1e at the podosome core became significantly decreased (Figure 2, F and G, and Supplemental Figure S3, F and G).
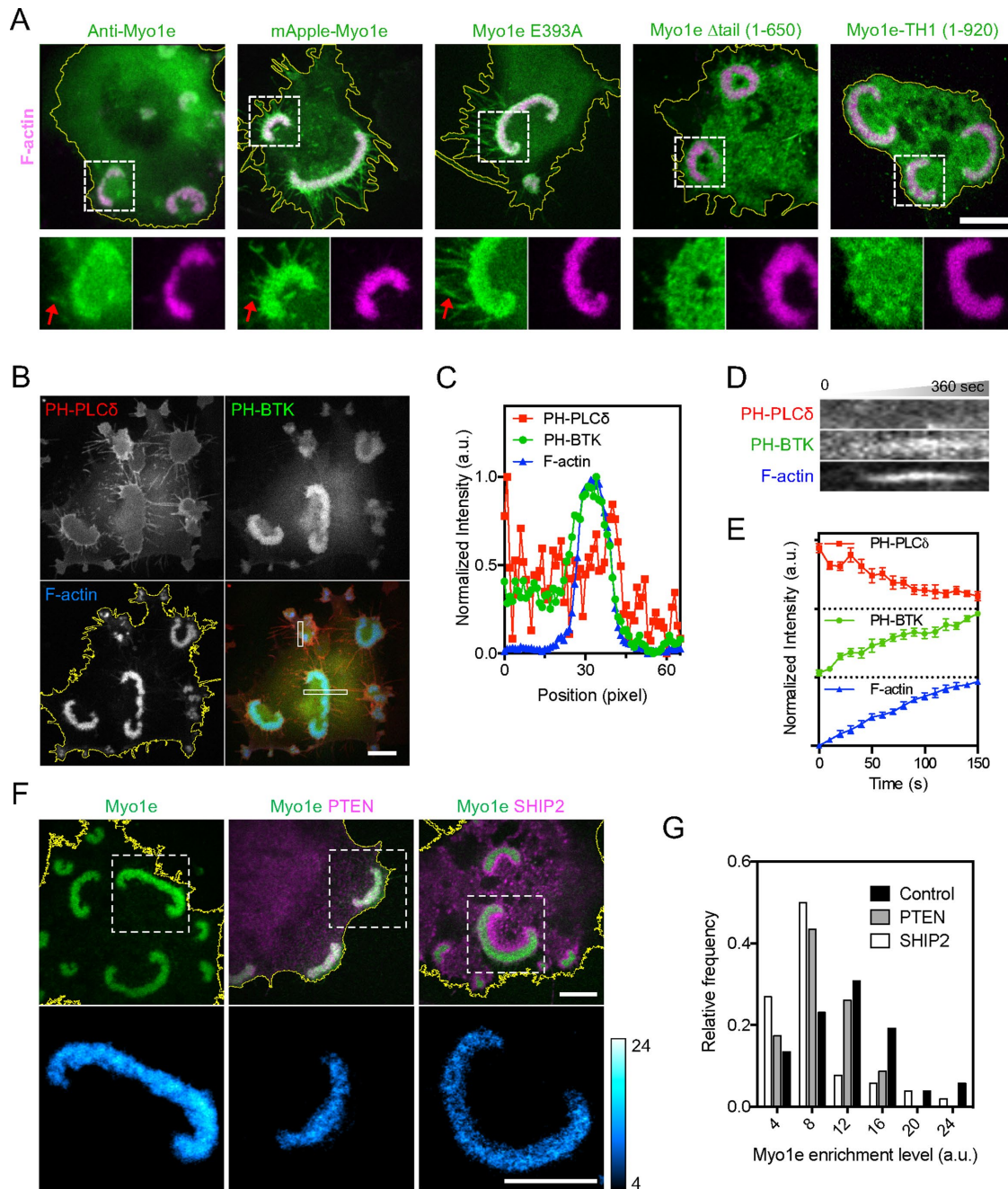
FIGURE 2: Myo1e localization at the podosome is dependent on the interaction between tail domains and PI(3,4,5)P3 lipids. (A) Endogenous Myo1e, mApple-tagged Myo1e, and motor domain mutated Myo1e E393A are enriched at the podosome and filopodia protrusion (red arrow) in MEF-Src. Myo1e without the tail domain (Myo1e Δtail, 1–650) and Myo1e-TH1 (1–920) fail to localize to the podosome. Inset, the boxed region (10×10 μm²). (B) PH-BTK-GFP (PI(3,4,5)P3 probe), not mCherry-PH-PLCδ (PI(4,5)P2 probe), is enriched at the podosome. (C) Intensity line scan of lipid probes (along the horizontal stripe in B). PH-BTK, not PH-PLCδ, are enriched at the actin-rich podosome. (D, E) Kymographs (along the vertical stripe in B) and normalized intensity-time plot of PH-PLCδ and PH-BTK. During the podosome formation, the PH-BTK level increases while the PH-PLCδ level slightly decreases ($n = 9$). (F) mApple-Myo1e enrichment level at the podosome drops when phosphatidylinositol phosphatase GFP-PTEN and GFP-SHIP2 are expressed. Inset, Myo1e in the boxed regions (20×20 μm²). Ratiometric images represent the enrichment level of Myo1e. (G) Histograms of Myo1e enrichment levels in F. Statistical information is in Supplemental Figure S3G. Error bars represent SEM. Scale bars represent 10 μm.

Overexpression of PTEN also resulted in reductions of Myo1e enrichment (Supplemental Figure S3G). These observations suggest that PI(3,4,5)P3 lipids are the key phosphatidylinositol lipids to recruit Myo1e to the podosome.

Myo1e's TH12 domain is the key motif responsible for plasma membrane association

The carboxy terminus of Myo1e consisted of three tail homologous domains (Figure 3A). We further examined the membrane
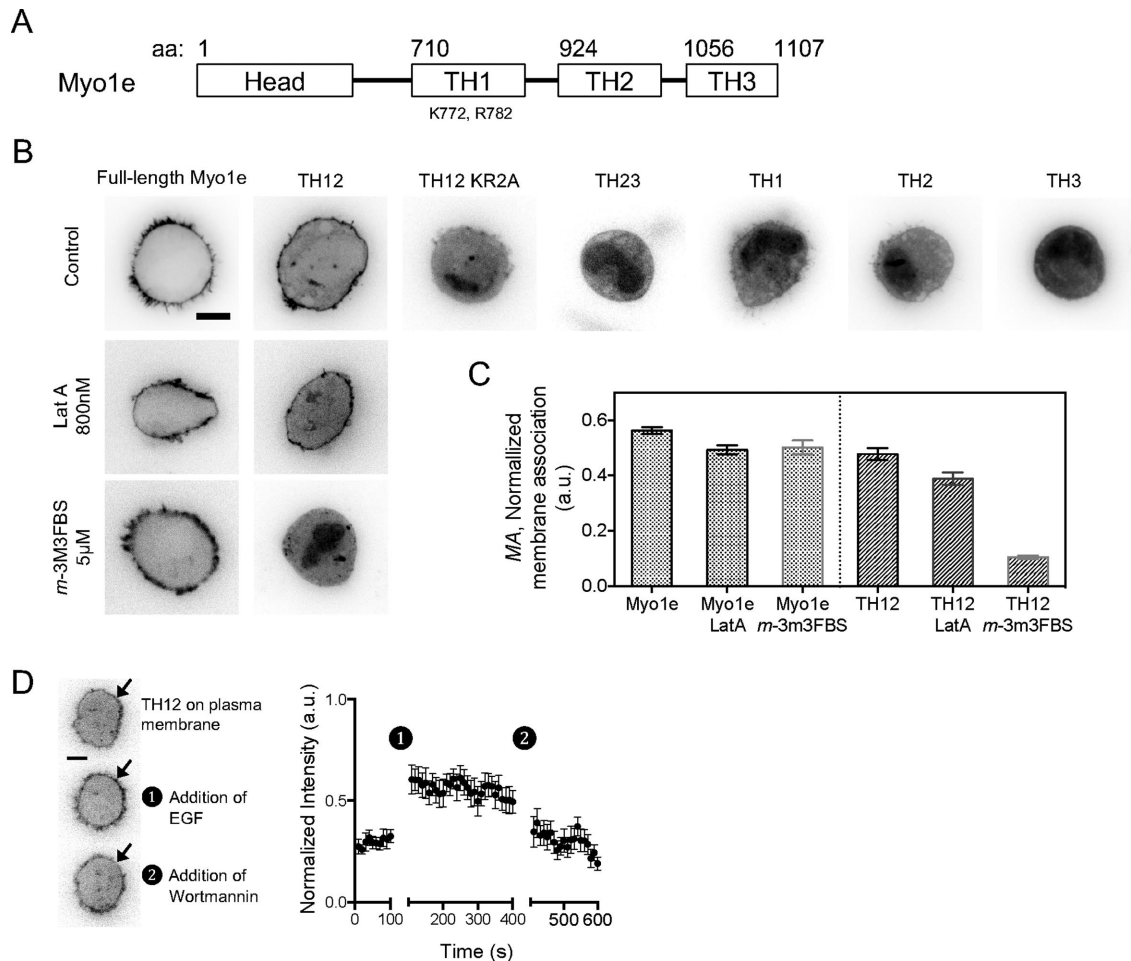
FIGURE 3: TH12 of Myo1e is the key domain responsible for plasma membrane association. (A) Domain diagram of Myo1e. (B) Inverted images of REF52 fibroblast cells with various Myo1e constructs. Images are taken at the plane of the great circle to evaluate the association to the plasma membrane. GFP-TH12, not GFP-TH12 KR2A, is recruited to the plasma membrane. (C) Membrane association analysis of Myo1e tails. TH12 loses the membrane association when PI(4,5)P2 lipids are depleted by *m*-3M3FBS. Statistical information is in Supplemental Figure S4E. (D) Epidermal growth factor (EGF; 100 ng/ml) stimulates the membrane association of GFP-TH12 (black arrows). Subsequent PI3K inhibition by Wortmannin (200 nM) causes TH12 to return to the original level on the plasma membrane (*n* = 14). Error bars represent SEM. Scale bars represent 10 μm.

association of full-length Myo1e and each Myo1e tail domain in non-transformed fibroblast cells. The great circle plane of each cell in suspension was imaged by confocal microscopy, and the normalized membrane association (*MA*, a self-defined parameter) was analyzed accordingly (Supplemental Figure S4A). We found that TH12 (TH1 and TH2) were enriched on the plasma membrane, while individual TH1, TH2, TH3, and TH23 were not (Figure 3B). TH12 with KR2A mutations (TH12 KR2A, K772 and R782 of full-length Myo1e both mutated to alanine [Feeser *et al.*, 2010]) failed to be recruited to the plasma membrane (Figure 3B). Inhibition of cortical F-actin assembly by latrunculin A (800 nM; Supplemental Figure S4B) resulted in a decrease of TH12 association on the plasma membrane (Figure 3, B and C, and Supplemental Figure S4E). Reduction of PI(4,5)P2 on the plasma membrane by phospholipase C activator *m*-3M3FBS (5 mg/ml; Supplemental Figure S4C) caused a prominent dissociation of TH12 from the plasma membrane (Figure 3, B and C, and Supplemental Figure S4E). Dual inhibition by latrunculin A and *m*-3M3FBS disrupted the plasma membrane association of full-length Myo1e (Supplemental Figure S4D). It is known that PI3K activation triggered by epidermal growth factor (EGF) can cause the production of

PI(3,4,5)P3 lipids on the plasma membrane. In live cells, the level of TH12 on the plasma membrane increased upon the stimulation of EGF (100 ng/ml; Figure 3D). The level of TH12 subsequently returned to the prestimulated level after PI3K inhibitor Wortmannin (200 nM) was introduced. Apart from binding to F-actin at the cell cortex, it appears that TH12 of Myo1e is the key domain to interact with both PI(4,5)P2 and PI(3,4,5)P3 lipids on the plasma membrane.

TH12 defines spatiotemporal dynamics of Myo1e at the ventral layer of podosome

Point mutations of KR2A were located in the PH-domain–containing TH1 domain of Myo1e, and TH12 KR2A was not associated with the plasma membrane. Full-length Myo1e with KR2A mutation (Myo1e KR2A) was also weakly associated with the plasma membrane and filopodia protrusions in the outer region of the podosome arc (Figure 4A and Supplemental Figure S5A). However, we found that Myo1e KR2A remained localized at the podosome core in MEF-Src. When we compared the axial distribution between Myo1e and Myo1e KR2A, the axial distribution of Myo1e KR2A did not exhibit ventral enrichment and was rather similar to the distribution of
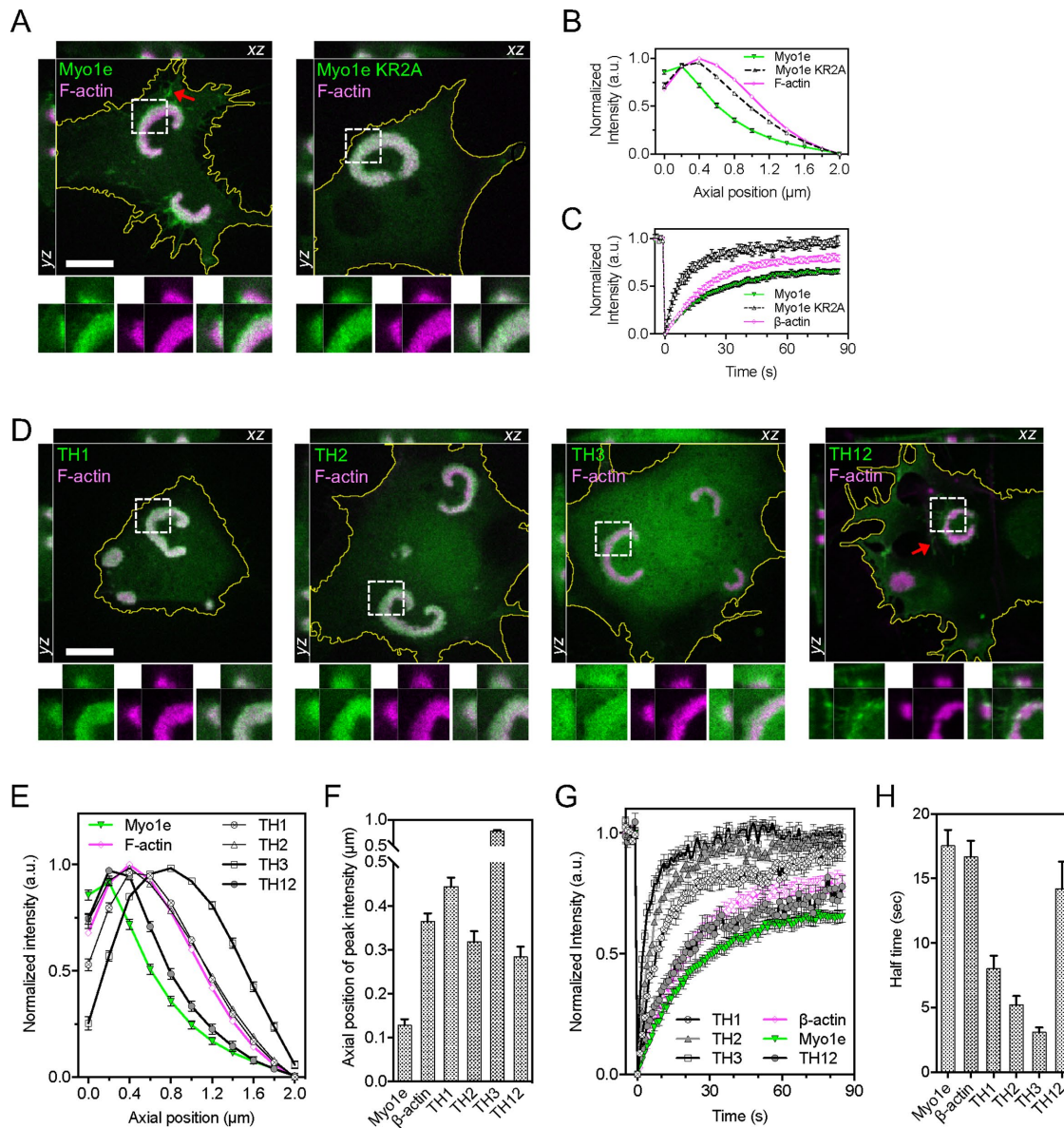
FIGURE 4: The ventral enrichment and slow recovery of Myo1e at the podosome is governed by TH12 domain. (A) Confocal images of GFP-Myo1e and GFP-Myo1e KR2A. Myo1e, not Myo1e KR2A, exhibits ventral enrichment at the podosome and membrane association at the filopodia protrusion (red arrow). Inset, the boxed region (7×7 µm²). (B) Axial distribution analysis of Myo1e and Myo1e KR2A at the podosome core. The distribution of Myo1e KR2A shifts away from the ventral layer of the podosome. (C) Intensity recovery curves after spot photobleaching at the podosome core. Myo1e exhibits slower recovery, while the recovery of Myo1 KR2A is faster. (D) Confocal images of GTP-tagged TH1, TH2, TH3, and TH12 at the podosome arc. While all of them localize to podosome, only TH12 exhibits ventral enrichment and membrane association at the filopodia protrusion (red arrow). Inset, the boxed region (7×7 µm²). (E, F) Axial distributions and peak positions of Myo1e tail domains at the podosome core. Statistical information is in Supplemental Figure S5B. (G, H) Intensity recovery curves and half-time of recovery of Myo1e tail domains after spot photobleaching at the podosome core. Among all other tail domains, only TH12 exhibits slow recovery dynamics. Statistical information is in Supplemental Figure S5C. Error bars represent SEM. Scale bars represent 10 µm.

F-actin (Figure 4B and Supplemental Figure S5B). We further examined the temporal dynamics of wild-type Myo1e, Myo1e KR2A, and β-actin at the podosome core by fluorescence recovery after photobleaching (FRAP). The recovery half-time of polymerized β-actin, the main structural component of the podosome core, was 16.67 ± 1.24 s (Figure 4C and Supplemental Figure S5C). The recovery half-time of Myo1e was similar to that of β-actin and was distinctly longer than that of Myo1e KR2A (17.53 ± 1.23 and 7.68 ± 1.14 s, respectively).

The fast recovery of Myo1e KR2A indicates a weak association with the plasma membrane at the podosome. Conversely, the slow dynamics of recovery indicates the confined diffusion of Myo1e at the interface between actin and the plasma membrane at the podosome core.

The lack of ventral enrichment and atypical FRAP dynamics of Myo1e KR2A suggested that other domains of Myo1e may contribute to the enrichment at the podosome in a lipid-independent

manner. Indeed, we further investigated the spatial-temporal dynamics of Myo1e tail domains and found that TH1, TH2, and TH3 alone were also enriched at the podosome core (Figure 4D). However, none of them exhibited ventral enrichment (Figure 4, E and F, and Supplemental Figure S5B). In addition, FRAP analysis revealed that individual TH1, TH2, and TH3 at the podosome core exhibited fast recovery after photobleaching, which distinctly differed from full-length Myo1e (Figure 4, G and H, and Supplemental Figure S5C). In nontransformed fibroblast, we found that TH1 and TH2 were recruited to F-actin stress fibers (Supplemental Figure S6, A and B), while TH12 was mainly located on the plasma membrane (Supplemental Figure S6C). Axial distributions of TH12 in MEF-Src exhibited ventral enrichment (Figure 4, D–F), and FRAP dynamics of TH12 also exhibited slow recovery (Figure 4, G and H, Supplemental Figure S5C, and Supplemental Movie 3). At the ventral layer, we further analyzed the lateral distribution of Myo1e and its tail domains across the podosome. Only Myo1e and TH12 showed membrane-proximal enrichment (Supplemental Figure S6, D and E). Therefore, TH12 defines the unique ventral-proximal distribution and temporal dynamics of Myo1e at the podosome core.

TH12-PI(3,4,5)P3 interaction hinders F-actin polymerization and podosome arc formation

Negatively charged phosphatidylinositol lipids, such as PI(4,5)P2 and PI(3,4,5)P3, can activate N-WASP and promote F-actin polymerization (Papayannopoulos et al., 2005). As our data of PH-domain probe distributions revealed that PI(3,4,5)P3, not PI(4,5)P2 lipids were locally enriched at the podosome, we examined whether the interaction between TH12 and PI(3,4,5)P3 can alter lipid-mediated F-actin polymerization. In MEF-Src, PH-BTK (PI(3,4,5)P3 probe) and N-WASP were enriched at the podosome core, and prominent F-actin polymerization repeatedly merged to form large F-actin arcs and rosettes (Figure 2B, Supplemental Figure S2M, and Supplemental Movie 2). However, when TH12 was introduced, the enrichment levels of PH-BTK and N-WASP at the podosome in TH12 expressing MEF-Src were lower as compared with lipid-binding mutant TH12 KR2A (Figure 5, A–F, and Supplemental Figure S7, A and B). In particular, the enrichment of PH-BTK and TH12 exhibited in a mutual-exclusive pattern (Supplemental Figure S7C). F-actin polymerization at the podosome became short-lived and unstable (Figure 5, G and H, Supplemental Figure S7D, and Supplemental Movie 4), and the formation of podosome arcs/rosettes were suppressed when TH12 was overexpressed. Overexpressing TH123 (full tail, TH12 and TH3 together) and blocking PI(3,4,5)P3 production by PI3K inhibitor Wortmannin (200 nM) resulted in similar suppression of podosome arc/rosette formation (Figure 5I and Supplemental Figure S7E).

While TH12 was found at short-lived podosomes, the spatial-temporal pattern of TH12 recruitment and F-actin polymerization was rather different. In the initial phase of podosome formation, the level of TH12 increased before N-WASP, Arp3, and F-actin (Figure 5, J and K, yellow triangles, and Supplemental Figure S7, F and G). The level of TH12 then started to decrease and fluctuate as the level of F-actin continued to increase (Supplemental Figure S7H). During the depolymerization phase of F-actin in the short-lived podosome, the level of TH12 persisted and subsequently decreased after podosome disassembly (Figure 5K, red triangles). On the contrary, the levels of lipid-binding mutant TH12 KR2A and F-actin were progressively increased and then decreased throughout the podosome formation (Supplemental Figure S7I). It appears that TH12 interacts with upstream lipid-mediated signals and impedes F-actin polymerization at the podosome.

TH12 suppresses podosome formation in RAW264.7 macrophages and matrix degradation in A375 melanoma cells

RAW264.7 macrophage cells natively formed dot-like podosomes as the adhesion structure on the extracellular matrix. Multiple podosomes were often found in each macrophage cell. Myo1e was localized with F-actin at the core of each podosome and surrounded by integrin adaptor proteins, such as paxillin (Figure 6A). F-actin assembly of macrophage podosomes usually have a lifetime of 50–200 s (Figure 6C and Supplemental Movie 5). When TH12 was expressed, the number of podosomes per cell was largely suppressed, as compared with full-length Myo1e (Figure 6, A and B, and Supplemental Figure S8A). The lifetime of F-actin assembly in TH12-expressing macrophage cells also became shorter, as compared with full-length Myo1e (Figure 6C, Supplemental Figure S8B, and Supplemental Movie 6). On the other hand, the lipid-binding mutant TH12 KR2A did not suppress the number of podosome in macrophages, and F-actin assembly of podosomes remained unperturbed (Supplemental Figure S8, C and D). Likewise, invadopodia assembly in cancer cells, such as A375 melanoma cell, exhibited similar cytoskeletal components as podosomes and locally degraded extracellular matrices (Supplemental Figure S9A). Myo1e was found at the core of invadopodia where the underlying Cy3-labeled gelatin matrix was degraded (Figure 6D). In TH12-expressing A375 cells, invadopodia formation was suppressed (Figure S9B), and the area of gelatin degradation was decreased (Figure 6, D and E, and Supplemental Figure S9C). In addition, the migration speed of A375 cells was reduced when TH12 was expressed (Figure 6F and Supplemental Figure S9D).

DISCUSSION

Podosomes are integrin-mediated adhesions with distinct three-dimensional F-actin organization. The regulation of F-actin polymerization plays a critical role in podosome assembly. Here, we quantitatively examine axial distributions of F-actin–binding proteins and regulators at the podosome. Among all 26 actin regulators we have examined, we find that long-tailed Myo1e is uniquely enriched at the ventral layer of the podosome. We also utilize photoconversions of cytosolic mEOS2-β-actin to reveal the spatial-temporal incorporation of newly converted β-actin into a preexisting podosome core. We find that F-actin polymerization takes place in the ventral layer of the podosome. Previous studies have reported that Myo1e interacts with actin filament nucleating factors N-WASP/WIP complexes and uncapping protein CARMIL (Edwards et al., 2014). Our previous work also indicated that Myo1e guides F-actin assembly inside the lamellipodia during the cell spreading process (Gupta et al., 2013). The axial distribution analysis of podosome core components reveals the molecular organization at different layers of the podosome. In particular, we compare various actin regulators in groups, such as G-actin–binding, filament nucleating, capping, depolymerizing, and cross-linking (Siripala and Welch, 2007; Pollard, 2016). At the ventral layer of the podosome, actin filament nucleating (Arp3, CARMIL, cortactin, and WIP) barbed-end capping (EPS8, CD2AP, and CapZ-beta2) are markedly enriched. Likewise, pointed-end capping protein TMOD3 is spatially enriched in the apical region of the F-actin core in the podosome. Disparate distributions of barbed-end capping and pointed-end capping proteins confirm the proximity of barbed-end filaments to the plasma membrane and overall orientations of pointed-end filaments toward the cytosol. Along with the ventral assembly of F-actin at the podosome, our observations suggest that Myo1e is positioned as the building block of signal
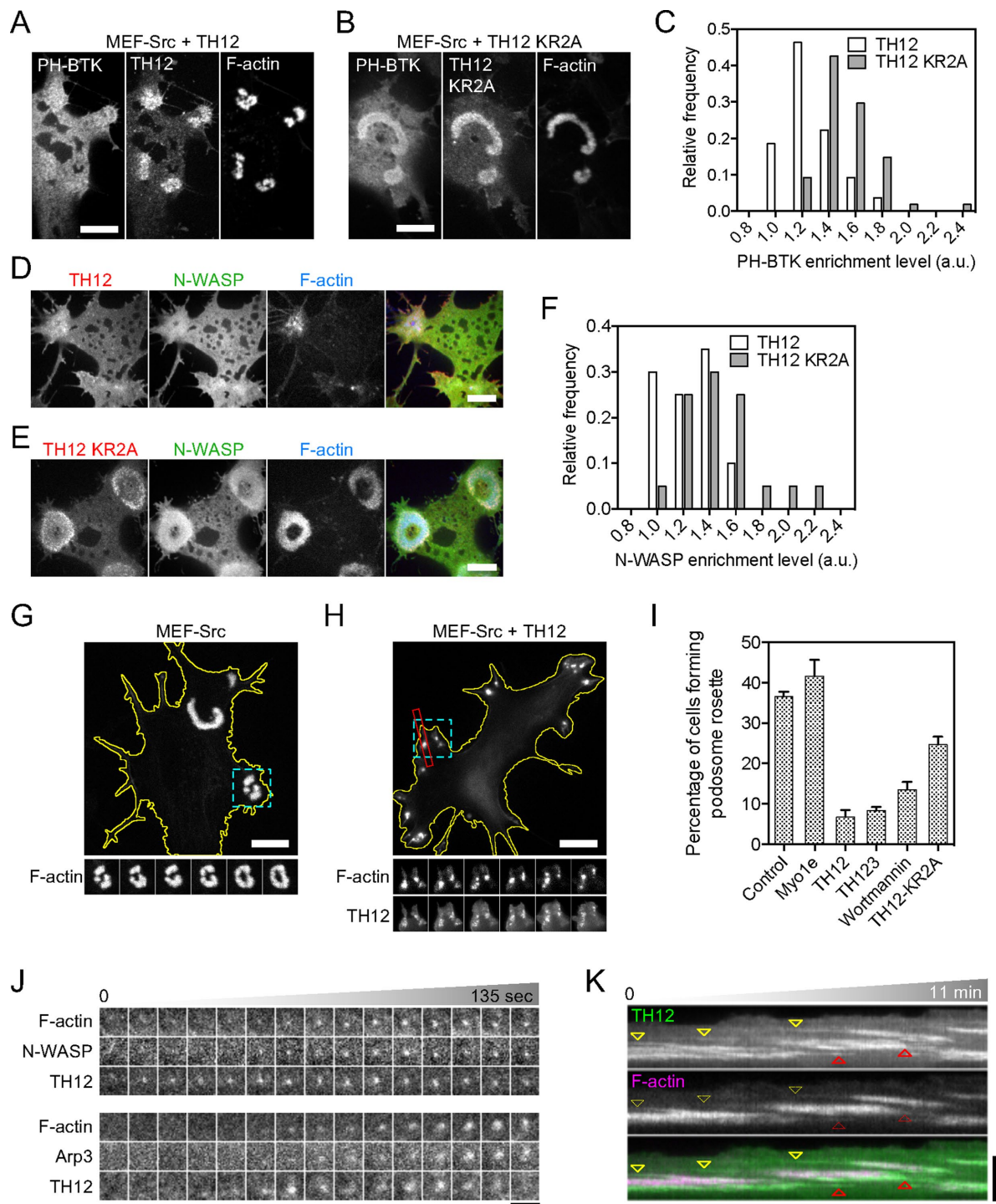
FIGURE 5: TH12 inhibits podosome arc assembly by interfering with PI(3,4,5)P3-mediated F-actin polymerization. (A, B) The enrichment level of PH-BTK-mRuby2 at the podosome decreases when GFP-TH12, not GFP-TH12 KR2A, is expressed. (C) Histograms of PH-BTK enrichment levels in A and B. Statistical information is in Supplemental Figure S7A. (D, E) The enrichment level of GFP-N-WASP at the podosome core is suppressed by the expression of EBFP2-TH12, not EBFP2-TH12 KR2A. (F) Histograms of N-WASP enrichment levels in D and E. Statistical information is in Supplemental Figure S7B. (G, H) The formation of podosome rosettes in MEF-Src. TH12-expressed MEF-Src lacks podosome rosettes and exhibits unstable and short-lived F-actin dots (marked by EBFP2-UtrCH). Inset, the cyan boxed region with 100-s time interval (10 × 10 µm²). (I) Podosome rosettes are suppressed by expression of TH12, TH123, and PI3K inhibitor Wortmannin (200 nM). Statistical information is in Supplemental Figure S7E. (J) TH12 precedes N-WASP and Arp3 in the initial phase of F-actin polymerization during the assembly of podosome. Each box represents 3 × 3 µm². (K) Kymographs of GFP-TH12 and EBFP2-UtrCH (F-actin marker) along the red stripe in H. TH12 appears before F-actin polymerization in the beginning of the podosome (yellow triangles) and remains after F-actin disassembly (red triangles). Error bars represent SEM. Scale bars represent 3 µm (J) and 10 µm (the rest).
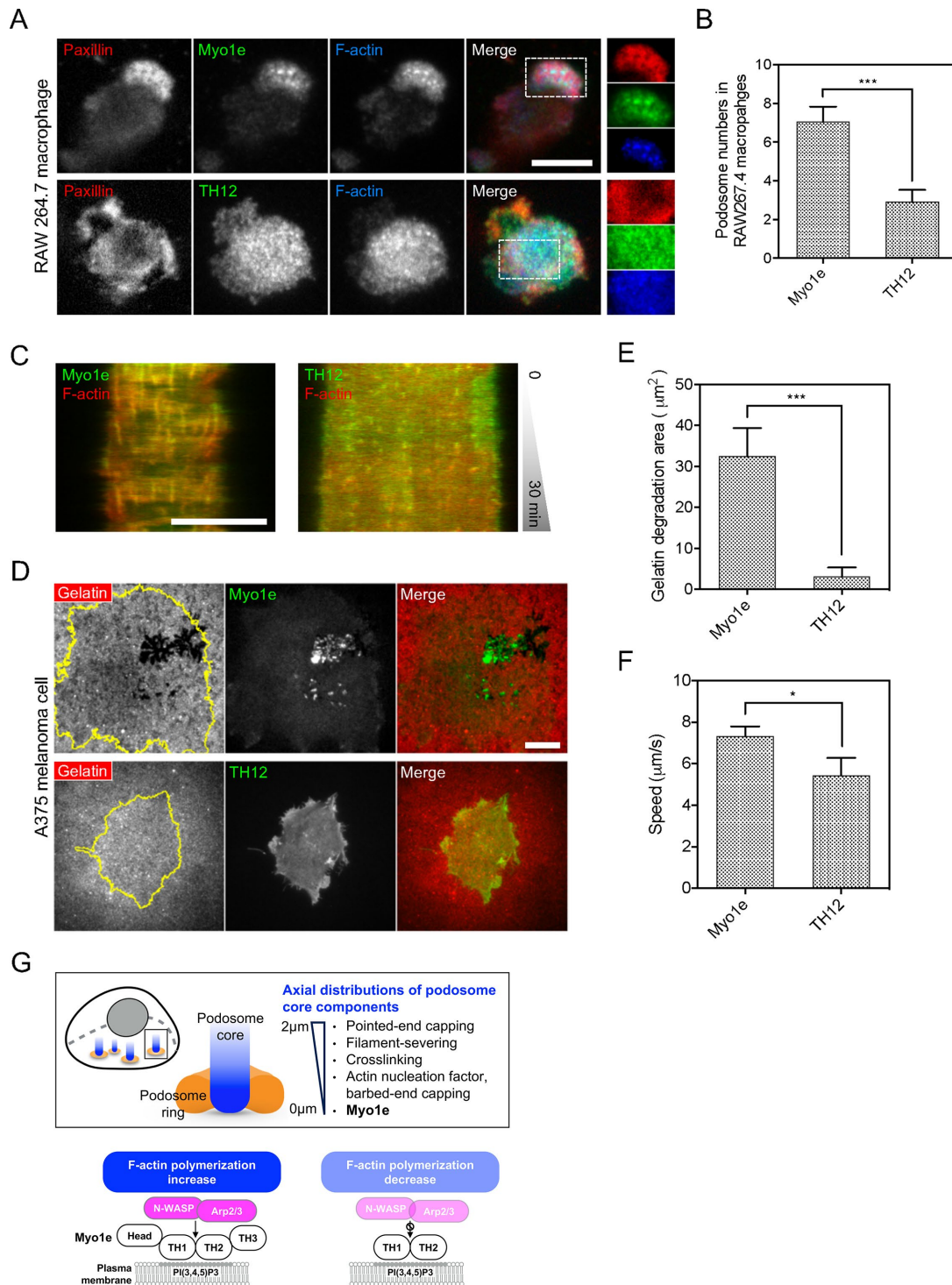
FIGURE 6: TH12 suppresses podosome formation and gelatin degradation. (A) RAW 264.7 macrophages form multiple podosomes. Each podosome consists of an F-actin core (CF680-phalloidin) and a ring (anti-paxillin). mApple-Myo1e is localized at the podosome core. TH12-expressing macrophages lack podosomes. Inset, the boxed region (10 × 6.7 µm²). (B) Macrophages assemble fewer podosomes when TH12 is expressed. Statistical information is in Supplemental Figure S8A. (C) Kymographs of full-length Myo1e and TH12 in macrophages. F-actin polymerization in TH12-expressing macrophage is short-lived and unstable. (D, E) A375 melanoma cells degrade Cy3-labeled gelatin substrates. mApple-Myo1e is locally enriched at the degraded region. When GFP-TH12 is expressed in A375 cells, the area of gelatin degradation decreases. Statistical information is in Supplemental Figure S9C. (F) Expression of TH12 in A375 melanoma cells reduces the migration speed on collagen-coated substrate. Statistical information is in Supplemental Figure S9D. (G) Schematic model of layered organization of podosome. Polymerizations of G-actin at the podosome core take place in a bottom-up manner. Myo1e is located at the ventral layer of the podosome and regulates PI(3,4,5)P3-mediated F-actin polymerization. P values by an unpaired t test are ***, P < 0.001 and *, P < 0.05. Error bars represent SEM. Scale bars represent 10 µm.

transductions between the plasma membrane and F-actin cyto-skeleton (Figure 6G).

Myo1e without the tail domain (Myo1e Δtail, 1-650) and Myo1e-TH1 (1-920) fail to localize to the podosome. Tail domains of long-tailed Myo1e exhibit important roles in various cellular processes, including membrane interaction and adhesion formation (Krendel *et al.*, 2007; Cheng *et al.*, 2012; Gupta *et al.*, 2013; Heim *et al.*, 2017). In all myosin1 isoforms, the tail domain is believed to play important roles in membrane association and ATP-insensitive F-actin binding (Lee *et al.*, 1999; Brzeska *et al.*, 2014). The membrane association of TH1 has been validated in short-tailed (such as Myo1c; Hokanson *et al.*, 2006) and nonmammalian myosin1 iso-forms (*Dictyostelium* myosin IE; Chen *et al.*, 2012). However, our data indicate that TH1 of mammalian Myo1e is not sufficient for membrane association. TH2 and TH3 domains are unique features in long-tailed myosin1 and are absent in other short-tailed myosin1 isoforms. TH2 of long-tailed myosin-I is shown to bind to F-actin in an ATP-independent manner (Jung and Hammer, 1994), and loss of TH2 may potentially cause the misfolding of TH1 (Lee *et al.*, 1999). TH3 of Myo1e contains a SH3 domain to facilitate protein–protein interactions (Krendel *et al.*, 2007). Nevertheless, TH2 and TH3 are not associated to the plasma membrane, either.

It is reported that negatively charged lipids, such as 2% of PI(4,5)P2 or 2% of PI(3,4,5)P3 lipids can recruit the tail domain TH123 of mammalian Myo1e to the model membrane vesicle in vitro (Feeser *et al.*, 2010). Our data further indicate that the combination of TH1 and TH2 (TH12) is the functional unit for membrane association. Mutations of K772A and R782A of TH12 result in the dissociation from the plasma membrane. Removing PI(4,5)P2 lipids by *m*-3M3FBS causes TH12 to dissociate from the plasma membrane. In addition, production of PI(3,4,5)P3 lipids by EGF stimulation pro-mote TH12 enrichment to the plasma membrane. These observa-tions indicate that TH12 of Myo1e can associate with the plasma membrane via both PI(4,5)P2 and PI(3,4,5)P3 lipids. Nevertheless, PI(3,4,5)P3, not PI(4,5)P2 lipids are progressively enriched during the podosome formation. It is known that SHIP2 can dephosphorylate the 5 position (D5) of the inositol head group of PI(3,4,5)P3 and PI(4,5)P2 lipids, and PTEN can dephosphorylate at the 3 position (D3) of the inositol head group of of PI(3,4,5)P3 and PI(3,4)P2 lipids. Dephosphorylation of PI(3,4,5)P3 lipids by SHIP2 or PTEN results in the reduction of Myo1e enrichment at the podosome. It appears that PI(3,4,5)P3 lipids are the key phosphatidylinositol species re-sponsible for Myo1e recruitment at the podosome. Further investi-gations reveal that TH12 serves as the key domain of Myo1e to in-teract with the plasma membrane and exhibits similar spatiotemporal characteristics at the podosome, including ventral enrichment, slow recovery dynamics after photobleaching, and membrane-proximal localization. Lipid-binding mutant Myo1e KR2A may be recruited to the podosome via TH2 (F-actin binding) or TH3 (SH3-PRD protein interaction), as it lacks the characteristics of ventral-proximal distri-bution and slow FRAP dynamics at the podosome.

Negatively charged lipids, such as PI(3,4,5)P3 can serve as an upstream signal to activate N-WASP and Cdc42 (Insall and Weiner, 2001; Papayannopoulos *et al.*, 2005), which trigger Arp2/3-medi-ated F-actin polymerization at the ventral layer of the podosome. As TH12-expressing MEF-Src cells often lack stable podosome arcs/rosettes, we hypothesize that overexpression of TH12 interferes with F-actin polymerization by competing local PI(3,4,5)P3-mediated sig-nals. Indeed, we find that the levels of PH-BTK (a PI(3,4,5)P3 probe) and N-WASP are negatively correlated with TH12 expression, but not the lipid-binding mutant TH12 KR2A. Likewise, in the initial phase of podosome formation, TH12, not TH12 KR2A, precedes

F-actin polymerization factor N-WASP and Arp3. The antagonized fluctuations between TH12 and F-actin polymerization factors sug-gest their competition for upstream PI(3,4,5)P3-mediated signals that are essential for podosome formation.

In agreement with the inhibitory characteristics of TH12 in MEF-Src, TH12 expression also blocks the podosome formation in RAW264.7 macrophages and suppresses the gelatin degradation and migration speed in A375 melanoma cells. TH123, which com-prises TH12 and TH3, has been demonstrated to interact with vari-ous proline-rich domain (PRD) containing proteins, such as WIP and N-WASP (Geli *et al.*, 2000; Cheng *et al.*, 2012). While WIP and N-WASP can promote F-actin polymerization, expression of TH123 still suppresses the podosome formation in MEF-Src. On the other hand, overexpression of full-length Myo1e does not suppress podo-some formation. Those results suggest additional factors to regulate TH12 domain, such as binding-inhibition partners or intramolecular conformational changes (Ishikawa *et al.*, 2004). It is known that the SH3P2 can bind to Myo1e tail and inhibit the Myo1e recruitment to the tip of lamellipodia (Tanimura *et al.*, 2016). The interaction of SH3P2 and TH12 remains to be investigated. Interactions between the motor domain and the cortical F-actin network on the plasma membrane are also speculated, as full-length Myo1e remains at the plasma membrane after *m*-3M3FBS treatment. The additional coupling with F-actin of full-length Myo1e may cause intramolecular conformational changes and alter the interaction between TH12 and the plasma membrane.

The expression and mutation of Myo1e have been linked to vari-ous diseases. The high expression level of Myo1e is associated with the decreased survival in patients with basal breast cancer (Hallett *et al.*, 2012). Knockdown of Myo1e in the mouse fibroblast results in the slower migration and unstable cell-matrix adhesions (Gupta *et al.*, 2013; Tanimura *et al.*, 2016). While knockout of Myo1e does not block tumor formation in the mouse model, loss of Myo1e delays breast tumor progression and suppresses lung metastasis (Ouderkirk-Pecone *et al.*, 2016). In addition, Myo1e-knockout mice lose the junc-tional integrity in the kidney podocyte cells (Bi *et al.*, 2013). Mutations of Myo1e have been discovered in various human diseases related to steroid-resistant nephrotic syndrome, including mutations at A159P, T119I, and Y695X (Mele *et al.*, 2011; Al-Hamed *et al.*, 2013). Podo-cytes with Myo1e mutations exhibit disruptions of membrane integ-rity in the glomerulus and cause protein leakages into the urine. While A159P and T119I mutations are within the motor domain, Y695X mutation results in loss of Myo1e tail domain. Here, our study reveals the mechanistic role of Myo1e tail domains in orchestrating the lipid-cytoskeleton interaction. We find that Myo1e is stably en-riched at the ventral layer of the podosome and interacts with PI(3,4,5)P3 lipids via its TH12 domain. Further studies are required to extend these findings to other physiological functions of Myo1e, including motor activation, cargo recognition, and adhesion regulation.

MATERIALS AND METHODS
Cell culture
RPTPα$^{+/+}$ mouse embryonic fibroblast (MEF) was a gift from Jan Sap, New York University. Rat embryonic fibroblast (REF52) was a gift from Benjamin Geiger, Weizmann Institute of Science, Rehovot, Israel. The A375 human melanoma cell was a gift from Martin Chi Hang Cheung, Faculty of Medicine, University of Hong Kong. MEF, REF52, and A375 cell lines were cultured in DMEM supplemented with 10% fetal bovine serum (FBS), 100 U/ml penicillin, 100 µg/ml streptomycin, and 3.7 g/l sodium bicarbonate and maintained in a 37°C incubator with 5% CO_2. The RAW264.7 macrophage cell line was obtained from the American Type Culture Collection. RAW264.7 macrophages

were cultured in DMEM supplemented with 11% FBS and maintained in a 37°C incubator with 5% CO_2. Phenol red–free DMEM was used as the live-cell imaging medium on the microscope.

Plasmid transfection and reagents

Full-length mApple-Myo1e (27698) was obtained from Addgene and subcloned into EGFP-C1 and EBFP-C1 vectors. Human Myo1e GFP-TH1 (710–923), GFP-TH2 (924–1055), GFP-TH3 (1056–1108), GFP-TH12, GFP-TH23, GFP-TH123, GFP-Myo1e E393A, GFP-Myo1e KR2A (K772A and R782A), GFP-Myo1e Δtail (1–650), mApple-Myo1e-TH1 (1–920), Lifeact-GFP, Lifeact-mRuby, RFP-paxillin, GFP-CARMIL1, GFP-N-WASP, GFP-filaminA, mCherry-vinculin, and Src-Y530F were used in our previous works (Gupta *et al.*, 2013; Yu *et al.*, 2013). TH12 KR2A (710–1055) from Myo1e KR2A was subcloned into EGFP-C1 and mRuby2-C1 vectors. Lifeact-EBFP2 and mEOS2-β-actin were gifts from Pakorn Kanchanawong, National University of Singapore, Singapore. mCherry-CAAX[KRas] was a gift from Jay T. Groves, University of California, Berkeley, CA. GFP-VASP and GFP-α-actinin1 were gifts from Alexander D. Bershadsky, Weizmann Institute of Science, Rehovot, Israel. GFP-CD2AP was a gift from Pascale Monzo, IFOM, the FIRC Institute of Molecular Oncology, Milan, Italy. GFP-fascin1 was a gift from Gareth E. Jones, Kings College London, UK. GFP-Mena was a gift from Sohail Ahmed, Institute of Medical Biology, A*STAR, Singapore. GFP-SHIP2 was a gift from Chistina Mitchell, Monash University, Australia. mCherry-EPS8 (29779), mCherry-Arp3 (27682), mCherry-WIP (29573), GFP-cortactin (26722), GFP-β-actin (31502), ABP1-RFP (27699), GFP-CapZ-beta2 (13298), Coronin1B-mCherry (27694), mCherry-cofilin1 (27687), Gelsolin-mCherry (37262), PH-BTK-GFP (51463), PH-PLCD1-GFP (51407), mCherry-PH-PLCδ (36075), GFP-UtrCH (26737), pLifeAct-miRFP703 (79993), pEYFP-C1-p85β (1408), mCherryC1-PIP5KI γ661 (29584), GFP-PTEN (10759), pDONR223-twinfilin1 (23651), pDest-EGFP-N1 (31796), and pDest-mCherry-N1 (31907) were obtained from Addgene. PH-BTK-mRuby2 was subcloned from PH-BTK-GFP. EBFP2-UtrCH was subcloned from GFP-UtrCH. GFP-PIK3CB (HsCD00036098), pENTR223-TMOD3 (HsCD00510268), pENTR223-plastin3 (HsCD00514272), pENTR223-arpin(HsCD00288605), pENTR223-profilin1 (HsCD00506237), pENTR223-CAP1 (HsCD00512313), and pENTR223-CAPG (HsCD00510206) were obtained from DNASU Plasmid Repository, Arizona State University, Tempe, AZ. pENTR223- and pDONR223-based plasmids were subcloned into pDest-EGFP-N1 and pDest-mCherry-N1 vectors using Gateway cloning protocol (Thermo Fisher Scientific). Electroporation (Neon transfection system; Life Technologies) was used to transfect plasmids into the cell. Cells were then used after 24–48 h of transfections. For fixed-cell experiments, cells were treated with freshly prepared paraformaldehyde (PFA, 4%), permeabilized with Triton X (0.05%), and blocked with bovine serum albumin (5%) overnight. Rabbit anti-myo1e (ab129789) antibody was obtained from Abcam. Mouse anti-paxillin (clone 349) was obtained from BD Biosciences Pharmingen. Alexa Fluor 555 conjugated anti-mouse secondary antibody (A-21422) was obtained from Thermo Fisher Scientific. CF405M-phalloidin (00034) and CF680R-phalloidin (00048) were obtained from Biotium.

Confocal fluorescence microscopy

An inverted spinning-disk confocal microscope (Perkin-Elmer Ultraview VoX; Yokogawa CSU-X1) with a piezo Z stage was utilized to visualize the podosome dynamics in MEF-Src cells. An electron-multiplying charge-coupled device (EMCCD) camera (Hamamatsu C9100-23B), 100× oil immersion lens (1.45 NA), and acousto-optic

tunable filter (AOTF)-controlled solid-state lasers (40–50 mW) were mounted on the microscope body (Nikon Eclipse Ti-E), and Volocity software (Perkin-Elmer) was used to control microscope acquisition. Typically, microscope settings of 100 ms exposure time, 250 EM gain, 200 nm z-step, and 10–20% of laser output were used to acquire z-stack images. An environmental chamber (37°C and 5% CO_2) was attached to the microscope body for long-term time-lapse imaging.

Total internal reflection fluorescence microscopy

An inverted total internal reflection fluorescence (TIRF) microscope (iLas2; Roper Scientific) was employed to visualize the podosome in macrophage and A375 cells. An EMCCD camera (Photometrics Evolve 512), 100× oil immersion lens (1.46 NA), and AOTF-controlled solid-state lasers (50–100 mW) were mounted on the microscope (Zeiss Axio Observer Z1), and MetaMorph (Molecular Devices) was used to control microscope acquisition. Typically, microscope settings of 100 ms exposure time, 800 EM gain, and 20–40% of laser output were applied. An environmental chamber (37°C and 5% CO_2) was attached to the microscope body for long-term time-lapse imaging.

Intensity analysis and image processing

ImageJ and Imaris software were employed to perform time-dependent intensity measurement. An F-actin channel was used to define the region of interest (ROI) of the podosome core via Wand tool (ImageJ) or Spot function (Imaris), and mean intensities of other channels within the ROI were measured accordingly. Mean intensities of camera background were measured in the area without cells, and mean intensities of cytosol background were measured in the cytosolic region away from the podosome. Kymographs were generated via the Reslice function in ImageJ. Volocity software (Perkin-Elmer) was used to create three-dimensional views (*xy*, *xz*, and *yz*) of z-stack images taken by a spinning-disk confocal microscope. The *xz* and *yz* views represent the cross-section of the podosome arc at the boxed region. For the purpose of presentation, each image was uniformly and unbiasedly processed to enhance the contrast and stored in TIF or ICS format.

Analysis of axial distribution at the podosome core

Multichannel z-stack images of MEF-Src cells were acquired with 200 nm per step along the *z*-axis by a spinning-disk confocal microscope. Images from 0 to 2 µm above the adhesion plane were used for the axial distribution analysis. An F-actin channel was used as the reference channel to identify podosomes. To compare different podosome components, acquired data sets were realigned by a home-written Matlab code so that the maximum fluorescence intensity in the F-actin channel was fixed at 400 nm above the adhesion plane. The z-stack image of F-actin at 400 nm above the substrate was used to define the ROI at the podosome core. Using a home-written ImageJ macro, mean intensities of the other podosome component within the ROI at all z-positions were measured respectively. After background subtraction, normalized axial distributions of each podosome component were plotted by GraphPad Prism. A self-defined parameter, *MaxZ*, represented the axial position of the highest intensity and was used to compare the axial distribution of each podosome component.

Photoconversion of cytosolic mEOS2-β-actin

MEF-Src cells were transfected with mEOS2-β-actin and pLifeAct-miRFP703 and imaged by a spinning-disk confocal microscope with a FRAP module (PhotoKinesis Unit, Perkin-Elmer Ultraview VoX). Photoswitchable mEOS2 changes the fluorescence

excitation/emission spectrum upon 405-nm laser activation. mEOS excitation/emission peaks are 505/516 nm before activation and become 569/581 nm after activation. Before spot activation, preconverted mEOS2-β-actins within the cell were photobleached by a 561-nm laser. Then, spot activation of a 405-nm laser was initiated over a small cytosolic region away from the podosome arc or other preexisting F-actin structures. After spot activation, a time-lapsed confocal image acquisition of a 561-nm channel with 200-nm z-step and 5-s interval was used to monitor the distribution of photoconverted mEOS2-β-actin in a preexisting podosome. As F-actin continues to polymerize at the podosome, newly converted mEOS2-β-actin away from the podosome can diffuse within the cytosol and then be assembled into F-actin structures at the different layers of the podosome core. The mean intensities of photoconverted mEOS2-β-actin within the ROI (podosome core, defined by pLifeAct-miRFP703) at each z position over time were measured by ImageJ software. The background intensity of the 561-nm channel was measured before photoactivation and subtracted accordingly.

Phosphatidylinositol-dependent enrichment of Myo1e at the podosome

Myo1e intensities at the podosome of MEF-Src overexpressed with PTEN (a phosphatidylinositol 3,4,5-trisphosphate 3-phosphatase) and SHIP2 (a phosphatidylinositol-3,4,5-trisphosphate 5-phosphatase) were acquired by a spinning-disk confocal microscope. PTEN and SHIP2 can dephosphorylate PI(3,4,5)P3 and generate PI(4,5)P2 and PI(3,4)P2, respectively. The mean intensities of mApple-Myo1e (I_{core}) were measured within the ROI (podosome core, defined by F-actin) at the ventral layer of the podosome (Supplemental Figure S3F). The mean intensities of camera background (I_{bkg}) were measured in the area without cells. To overcome expression variations, the mean intensities of cytosol background (I_0) of mApple-Myo1e were measured in the cytosolic region away from the podosome. The enrichment level of Myo1e, defined by $(I_{core} - I_0)/(I_0 - I_{bkg})$, was used to compare in a phosphatidylinositol-dependent manner.

Membrane association analysis

Membrane association levels of various tail constructs of Myo1e were measured in nontransformed REF52 fibroblasts. Myo1e tail constructs and a reference probe for plasma membrane (such as mCherry-CAAX^{KRas} or Lifeact-mRuby to mark cortical actin) were cotransfected via electroporation. After 24 h, cells were trypsinized and resuspended with Dulbecco's phosphate-buffered saline (DPBS) containing dimethyl sulfoxide (control), latrunculin A (800 nM), or m-3M3FBS (5 µM) for 30 min in a 37°C incubator. REF52 fibroblasts were used because a large number of MEFs were prone to generate membrane blebs during the resuspension. Cells were then fixed by 4% PFA for 30 min in 37°C and placed on a glass-bottom dish. Suspended cells were imaged near the plane of great circle by a spinning-disk confocal microscope and analyzed by a home-written ImageJ macro and Matlab code. Intensity profiles of Myo1e tail constructs were measured by an outside-in line scan (~10 µm long) across the plasma membrane (Supplemental Figure S4A). The maximum intensity (I_{max}), camera background (I_{bkg}), and cytosol background (I_0) were also measured accordingly. Normalized membrane association (MA), a self-defined parameter, was used to compare the membrane association of Myo1e tail constructs. $MA = (I_{max} - I_0)/(I_{max} - I_{bkg})$. A higher MA value suggested a higher level of plasma membrane association.

EGF stimulation and membrane enrichment

REF52 cells transfected with GFP-TH12 were serum-starved for 12 h and then placed on a noncoated glass-bottom dish in DPBS with CaCl$_2$ (2.5 µM). To follow the membrane association analysis above, REF52 fibroblasts were also used. Time-lapse images of TH12 were taken on a spinning-disk confocal microscope and focused ~5 µm above the cell-glass interface. EGF (100 ng/ml) was added to stimulate PI3K activation and PI(3,4,5)P3 production. Subsequently, Wortmannin (200 nM) was introduced to inhibit PI3K's function. The intensity changes of TH12 on the plasma membrane were analyzed by Imaris software.

FRAP

Podosome core components in MEF-Src were spot-bleached using a 488-nm laser (PhotoKinesis Unit; Perkin-Elmer Ultraview VoX spinning-disk confocal microscope). Images were taken every 1 s. The bleaching laser was activated at the sixth frames, and 100 images were collected in total. EBFP2-UtrCH was cotransfected and used as the nonbleachable reference channel to monitor and ensure podosome stability during the recovery process. Bleached spots were defined as a ROI, and the intensity recovery within the ROI was measured by a home-written ImageJ macro. After camera background and cytosol bleach correction, the recovered intensity profiles (y) over time (x) were normalized in GraphPad Prism and fitted with a model of single-phase association after bleaching, $y = y_p (1 - e^{k \cdot x})$. Two fitting parameters, y_p and k, were calculated. $(ln\,2)/k$ represented the half-time of recovery (Figure 4H and Supplemental Figure S5C).

Lateral distribution at the podosome core

Myo1e tail constructs and EBFP2-UtrCH (F-actin marker) were coexpressed in MEF-Src, and EBFP2-UtrCH was used as the reference to specify the lateral range of podosomes (Supplemental Figure S6D). Intensity profiles of F-actin and Myo1e tail constructs were measured by an outside-in line scan (~10 µm long) across each podosome and then analyzed by a home-written ImageJ macro and Matlab code. The peak position and peak intensity of the F-actin line scan profile were defined as $X_{p.actin}$ and $I_{Xp.actin}$, respectively. The SD of background intensity of cytosolic F-actin away from podosomes ($SD_{CYB.actin}$) was measured accordingly. Positions within the intensity values between $I_{X.actin\,p} - 3SD_{CYB.actin}$ and $I_{Xp.actin}$ were defined as the lateral range of the podosome. The outermost position of the podosome range was defined as $X_{f.actin}$, and zone1 (membrane proximal) represented the lateral position between $X_{f.actin}$ and $X_{p.actin}$. The innermost position of the podosome range was defined as $X_{r.actin}$, and zone2 (membrane distal) represented the lateral position between $X_{p.actin}$ and $X_{r.actin}$. This lateral range between $X_{f.actin}$ and $X_{r.actin}$ was then used to examine the distribution of various Myo1e tail constructs. The peak position and peak intensity of other Myo1e tail constructs was defined as X_p and I_{Xp}, respectively. The peak position ratio (PP), a self-defined parameter, was utilized to compare the lateral distribution of Myo1e tail constructs. $PP = (X_p - X_{f.actin})/(X_{r.actin} - X_{f.actin})$. A smaller PP value suggested the lateral enrichment in the outer region of the podosome (zone1, membrane proximal).

Analysis of PH-BTK and N-WASP levels at the podosome

MEF-Src cells with overexpression of TH12 or TH12 KR2A were used to reveal the TH12-dependent enrichment of PH-BTK and N-WASP at the podosome core. Similar to the quantification method of phosphatidylinositol-dependent enrichment of Myo1e, mean intensities of PH-BTK and N-WASP (I_{core}) were measured within the ROI (podosome core, defined by F-actin) at the ventral layer of the podosome (Supplemental Figure S3F). The mean intensities of camera background (I_{bkg}) were measured in the area without cells. To overcome expression variations, the mean intensities of cytosol background

(I_0) were measured in the cytosolic region away from the podosome. The enrichment level of PH-BTK or N-WASP at each podosome was then defined as (I_{core} − I_0)/(I_0 − I_{bkg}) + 1.

Gelatin degradation assays

Cy3-labeled gelatin (ECM671; Millipore) was prepared in DPBS and mixed with unlabeled gelatin at a mass ratio of 1:70. Mixed gelatin solution (0.3–0.4 mg/ml) was coated on a glass-bottom dish for 5 min. Excess gelatin solution was aspirated. Coated gelatin was cross-linked by glutaraldehyde (0.5%) for 1 min, rinsed three times with phosphate-buffered saline, and quenched in the cell culture medium overnight at 37°C. Before seeding cells, cross-linked gelatin substrate was coated with collagen-I (50 µg/ml, 30 min at 37°C), in order to promote cell adhesions. After 48 h, cells on the gelatin-coated substrate were fixed by 4% PFA and imaged by TIRF microscopy. The degraded areas, defined by the regions without Cy3-gelatin, were measured by ImageJ software.

Statistical information

Statistical graphs with the mean and error bars (standard error of the mean, SEM) were plotted by GraphPad Prism software. All data are representative of at least three independent experiments. Statistical significance analysis was performed by GraphPad Prism software.

REFERENCES

Al-Hamed MH, Al-Sabban E, Al-Mojalli H, Al-Harbi N, Faqeih E, Al Shaya H, Alhasan K, Al-Hissi S, Rajab M, Edwards N, et al. (2013). A molecular genetic analysis of childhood nephrotic syndrome in a cohort of Saudi Arabian families. J Hum Genet 58, 480–489.

Balla T (2013). Phosphoinositides: tiny lipids with giant impact on cell regulation. Physiol Rev 93, 1019–1137.

Bi J, Chase SE, Pellenz CD, Kurihara H, Fanning AS, Krendel M (2013). Myosin 1e is a component of the glomerular slit diaphragm complex that regulates actin reorganization during cell-cell contact formation in podocytes. Renal Physiol 305, F532–F544.

Brzeska H, Pridham K, Chery G, Titus MA, Korn ED (2014). The association of myosin IB with actin waves in dictyostelium requires both the plasma membrane-binding site and actin-binding region in the myosin tail. PLoS One 9, e94306.

Buccione R, Orth JD, McNiven MA (2004). Foot and mouth: podosomes, invadopodia and circular dorsal ruffles. Nat Rev Mol Cell Biol 5, 647–657.

Case LB, Waterman CM (2015). Integration of actin dynamics and cell adhesion by a three-dimensional, mechanosensitive molecular clutch. Nat Cell Biol 17, 955–963.

Castro-Castro A, Marchesin V, Monteiro P, Lodillinsky C, Rosse C, Chavrier P (2016). Cellular and molecular mechanisms of MT1-MMP-dependent cancer cell invasion. Annu Rev Cell Dev Biol 32, 555–576.

Cervero P, Himmel M, Kruger M, Linder S (2012). Proteomic analysis of podosome fractions from macrophages reveals similarities to spreading initiation centres. Eur J Cell Biol 91, 908–922.

Chen CL, Wang Y, Sesaki H, Iijima M (2012). Myosin I links PIP3 signaling to remodeling of the actin cytoskeleton in chemotaxis. Sci Signal 5, ra10.

Cheng J, Grassart A, Drubin DG (2012). Myosin 1E coordinates actin assembly and cargo trafficking during clathrin-mediated endocytosis. Mol Biol Cell 23, 2891–2904.

Di Paolo G, De Camilli P (2006). Phosphoinositides in cell regulation and membrane dynamics. Nature 443, 651–657.

Dyson JM, O'Malley CJ, Becanovic J, Munday AD, Berndt MC, Coghill ID, Nandurkar HH, Ooms LM, Mitchell CA (2001). The SH2-containing inositol polyphosphate 5-phosphatase, SHIP-2, binds filamin and regulates submembraneous actin. J Cell Biol 155, 1065–1079.

Edwards M, Zwolak A, Schafer DA, Sept D, Dominguez R, Cooper JA (2014). Capping protein regulators fine-tune actin assembly dynamics. Nat Rev Mol Cell Biol 15, 677–689.

El Azzouzi K, Wiesner C, Linder S (2016). Metalloproteinase MT1-MMP islets act as memory devices for podosome reemergence. J Cell Biol 213, 109–125.

Eyckmans J, Boudou T, Yu X, Chen CS (2011). A hitchhiker's guide to mechanobiology. Dev Cell 21, 35–47.

Feeser EA, Ignacio CM, Krendel M, Ostap EM (2010). Myo1e binds anionic phospholipids with high affinity. Biochemistry 49, 9353–9360.

Geli MI, Lombardi R, Schmelzl B, Riezman H (2000). An intact SH3 domain is required for myosin I-induced actin polymerization. EMBO J 19, 4281–4291.

Goley ED, Welch MD (2006). The ARP2/3 complex: an actin nucleator comes of age. Nat Rev Mol Cell Biol 7, 713–726.

Gupta P, Gauthier NC, Cheng-Han Y, Zuanning Y, Pontes B, Ohmstede M, Martin R, Knolker HJ, Dobereiner HG, Krendel M, Sheetz M (2013). Myosin 1E localizes to actin polymerization sites in lamellipodia, affecting actin dynamics and adhesion formation. Biol Open 2, 1288–1299.

Hallett RM, Dvorkin-Gheva A, Bane A, Hassell JA (2012). A gene signature for predicting outcome in patients with basal-like breast cancer. Sci Rep 2, 227.

Heim JB, Squirewell EJ, Neu A, Zocher G, Sominidi-Damodaran S, Wyles SP, Nikolova E, Behrendt N, Saunte DM, Lock-Andersen J, et al. (2017). Myosin-1E interacts with FAK proline-rich region 1 to induce fibronectin-type matrix. Proc Natl Acad Sci USA 114, 3933–3938.

Hokanson DE, Laakso JM, Lin T, Sept D, Ostap EM (2006). Myo1c binds phosphoinositides through a putative pleckstrin homology domain. Mol Biol Cell 17, 4856–4865.

Hoshino D, Jourquin J, Emmons SW, Miller T, Goldgof M, Costello K, Tyson DR, Brown B, Lu Y, Prasad NK, et al. (2012). Network analysis of the focal adhesion to invadopodia transition identifies a PI3K-PKCα invasive signaling axis. Sci Signal 5, ra66.

Hynes RO (2002). Integrins: bidirectional, allosteric signaling machines. Cell 110, 673–687.

Insall RH, Weiner OD (2001). PIP3, PIP2, and cell movement—similar messages, different meanings? Dev Cell 1, 743–747.

Ishikawa T, Cheng N, Liu X, Korn ED, Steven AC (2004). Subdomain organization of the Acanthamoeba myosin IC tail from cryo-electron microscopy. Proc Natl Acad Sci USA 101, 12189–12194.

Jung G, Hammer JA 3rd (1994). The actin binding site in the tail domain of Dictyostelium myosin IC (myoC) resides within the glycine- and proline-rich sequence (tail homology region 2). FEBS Lett 342, 197–202.

Krendel M, Osterweil EK, Mooseker MS (2007). Myosin 1E interacts with synaptojanin-1 and dynamin and is involved in endocytosis. FEBS Lett 581, 644–650.

Labernadie A, Bouissou A, Delobelle P, Balor S, Voituriez R, Proag A, Fourquaux I, Thibault C, Vieu C, Poincloux R, et al. (2014). Protrusion force microscopy reveals oscillatory force generation and mechanosensing activity of human macrophage podosomes. Nat Commun 5, 5343.

Lee WL, Ostap EM, Zot HG, Pollard TD (1999). Organization and ligand binding properties of the tail of Acanthamoeba myosin-IA. Identification of an actin-binding site in the basic (tail homology-1) domain. J Biol Chem 274, 35159–35171.

Lu Q, Li J, Ye F, Zhang M (2015). Structure of myosin-1c tail bound to calmodulin provides insights into calcium-mediated conformational coupling. Nat Struct Mol Biol 22, 81–88.

McConnell RE, Tyska MJ (2010). Leveraging the membrane—cytoskeleton interface with myosin-1. Trends Cell Biol 20, 418–426.

McIntosh BB, Ostap EM (2016). Myosin-I molecular motors at a glance. J Cell Sci 129, 2689–2695.

Mele C, Iatropoulos P, Donadelli R, Calabria A, Maranta R, Cassis P, Buelli S, Tomasoni S, Piras R, Krendel M, et al. (2011). MYO1E mutations and childhood familial focal segmental glomerulosclerosis. N Engl J Med 365, 295–306.

Murphy DA, Courtneidge SA (2011). The "ins" and "outs" of podosomes and invadopodia: characteristics, formation and function. Nat Rev Mol Cell Biol 12, 413–426.

Oikawa T, Itoh T, Takenawa T (2008). Sequential signals toward podosome formation in NIH-src cells. J Cell Biol 182, 157–169.

Ouderkirk JL, Krendel M (2014). Myosin 1e is a component of the invadosome core that contributes to regulation of invadosome dynamics. Exp Cell Res 322, 265–276.

Ouderkirk-Pecone JL, Goreczny GJ, Chase SE, Tatum AH, Turner CE, Krendel M (2016). Myosin 1e promotes breast cancer malignancy by enhancing tumor cell proliferation and stimulating tumor cell de-differentiation. Oncotarget 7, 46419–46432.

Papayannopoulos V, Co C, Prehoda KE, Snapper S, Taunton J, Lim WA (2005). A polybasic motif allows N-WASP to act as a sensor of PIP(2) density. Mol Cell 17, 181–191.

Park WS, Heo WD, Whalen JH, O'Rourke NA, Bryan HM, Meyer T, Teruel MN (2008). Comprehensive identification of PIP3-regulated PH domains from *C. elegans* to *H. sapiens* by model prediction and live imaging. Mol Cell 30, 381–392.

Pollard TD (2016). Actin and actin-binding proteins. Cold Spring Harb Perspect Biol 8, a018226.

Reubold TF, Eschenburg S, Becker A, Kull FJ, Manstein DJ (2003). A structural model for actin-induced nucleotide release in myosin. Nat Struct Biol 10, 826–830.

Schiller HB, Fassler R (2013). Mechanosensitivity and compositional dynamics of cell-matrix adhesions. EMBO Rep 14, 509–519.

Siripala AD, Welch MD (2007). SnapShot: actin regulators I. Cell 128, 626.

Takenawa T, Suetsugu S (2007). The WASP-WAVE protein network: connecting the membrane to the cytoskeleton. Nat Rev Mol Cell Biol 8, 37–48.

Tanimura S, Hashizume J, Arichika N, Watanabe K, Ohyama K, Takeda K, Kohno M (2016). ERK signaling promotes cell motility by inducing the localization of myosin 1E to lamellipodial tips. J Cell Biol 214, 475–489.

van den Dries K, Meddens MB, de Keijzer S, Shekhar S, Subramaniam V, Figdor CG, Cambi A (2013). Interplay between myosin IIA-mediated contractility and actin network integrity orchestrates podosome composition and oscillations. Nat Commun 4, 1412.

Yamaguchi H, Yoshida S, Muroi E, Yoshida N, Kawamura M, Kouchi Z, Nakamura Y, Sakai R, Fukami K (2011). Phosphoinositide 3-kinase signaling pathway mediated by p110α regulates invadopodia formation. J Cell Biol 193, 1275–1288.

Yu CH, Rafiq NB, Krishnasamy A, Hartman KL, Jones GE, Bershadsky AD, Sheetz MP (2013). Integrin-matrix clusters form podosome-like adhesions in the absence of traction forces. Cell Rep 5, 1456–1468.

Yu HY, Bement WM (2007). Multiple myosins are required to coordinate actin assembly with coat compression during compensatory endocytosis. Mol Biol Cell 18, 4096–4105.